DEFORMATION ANALYSIS OF POLYMER FOAMS UNDER COMPRESSION LOAD USING *IN SITU* COMPUTED TOMOGRAPHY AND FINITE ELEMENT SIMULATION METHODS

O. Weißenborn[1], S. Geller[1], M. Gude[1], F. Post[2], S. Praetorius[2], A. Voigt[2], S. Aland[2]

[1]Institute of Lightweight Engineering and Polymer Technology (ILK), TU Dresden, Holbeinstraße 3, 01307 Dresden, Germany, Web Page: http://tu-dresden.de/mw/ilk
[2]Institute of Scientific Computing (IWR), TU Dresden, Zellescher Weg 12-14, 01069 Dresden, Germany, Web Page: www.math.tu-dresden.de/wir

Corresponding author: oliver.weissenborn@tu-dresden.de,

Keywords: polymer foams, non destructive testing methods, in situ computed tomography, deformation behaviour, finite-element-model

Abstract
Since different X-ray tomographic techniques offer advantageous characteristics, they frequently complete or even replace standard methods based on acoustic emission, thermography and ultrasonic. Especially the detection and evaluation of voids and cellular structures can be performed with a resolution of up to 1 µm and 3D visualization. Within this paper, a novel in situ CT device is used to perform compression tests on closed-cell polymeric foams with a defined foam density. Next to the determination of the cell structure with consideration of the pore size distribution and their morphology, the elastic compression behaviour is investigated. Following the analysis of the foam structure, the implementation of an implicit Finite element model is developed based on computer tomographic scans. By the introduction of a phase field function to implicitly describe the foam structure, technical difficulties associated with meshing the complex structure can be avoided and the equations to describe the deformation behaviour are effectively solved on high performance computers. Beyond that, the results gained by the in situ CT device help to adapt and complete the currently available elastic deformation models and therefore offer the opportunity to predict the material behaviour for various load scenarios of polymeric foams.

1. Introduction

The damage analysis of composite materials along with the development of suitable material models has been one mayor research focus during the last decades. In this context, the use of non-destructive testing (NDT) methods is of vital importance to fully understand the damage phenomenology, such as crack initiation and growth [1, 2]. In the context of novel lightweight structures, polymer foams exhibit excellent potential for the use as core layers in sandwich beams or as matrix material for nanoparticle- [3], short- and long-fibre-reinforced composites [4]. Since the damage and deformation behaviour of foams is strongly dependent on their cellular morphology, the demand for efficient experimental and simulation methods to analyse and compute these complex microscopic structures is growing. Although the effective mechanical properties of polymer foams have been comprehensively investigated [5, 6], the localisation and calculation of local strains, which could lead to damage initiation spots, still remains a complicated issue. Within this paper, the in situ computed tomography was used to analyse the compression deformation behaviour of a polyurethane foam. The introduction of a phase-field function allows the calculation of local strains and the resulting material stiffness depending on the material porosity.

2. Materials

For mechanical and morphological characterization a two-component polyurethane system (Rühl Puromer GmbH, Friedrichsdorf, Germany) consisting of a polyetherpolyol (puropreg® 569IT) and a diphenylmethan-diisocyanate (puronate® 900) was used. The processing and mixing of the components was performed according to the manufacturer's formulation with a mixing ratio of 100:150 (Poly:Iso) using a high-pressure mixing head (KraussMaffei Technologies GmbH, Munich, Germany). The polyurethane mixture was discharged into a cavity, allowing the foam to expand and cure in the closed mould. After curing, the foam was demoulded and left for at least 24 h at room temperature for post-curing before preparing samples for mechanical testing. Cube-shaped specimen with an edge length of 10 mm were cut out of the middle of the foam block using a parting-off grinder with cooling and lubricant liquids to eliminate moulding skins. The resulting foam is characterized by a closed-cell structure with pore sizes of up to 200 µm. With the use of microscopic images taken from microsections and greyvalue analysis, the material volume fraction $\chi = 0.21$ was determined for the given foam density of 230 kg/m³.

3. Evaluation of the compression behaviour using in situ CT analysis

For experimental investigations an FCTS 160-IS testing machine with a 160 kV microfocus X-ray tube and a minimum focal spot of lower than 3 µm was used to evaluate the deformation behaviour of the microcellular foam structure under compression loading. The CT test device consists of a flat panel detector with 3.200 x 2.300 14 bit pixels whereat one pixel is 127 x 127 µm². Due to the large geometrical magnification, the maximal resolution of the CT is 1 µm. In contrast to conventional CT devices, the in situ CT unit rotates around the fixed specimen. The cubic foam specimens were tested in six steps ranging from the unloaded state until 10 % strain in thickness direction with a quasi-static testing velocity of 3 mm/min. By reaching the predefined deformation thresholds, the movement of the force transmission element pauses for 15 minutes to allow the CT device to scan the specimen structure while the foam structure is still loaded. In total, six different specimen were examined within this study to evaluate the mechanical properties, one was tested with the in situ CT device. The main purpose of the CT scan was to analyse the deformation behaviour as exact as possible and to generate input data for simulation studies. The compression behaviour reveals a linear-elastic correlation between stress and strain in the range of 0.5 to 2 % strain (Figure 1 left).
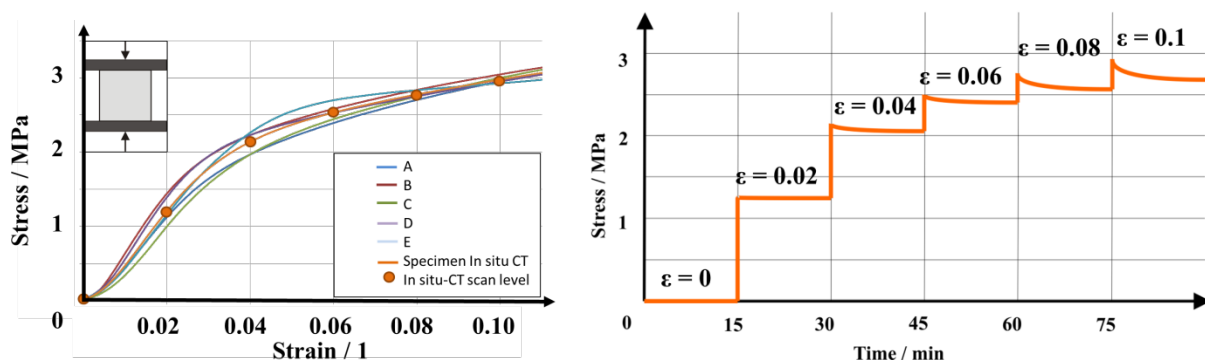
Figure 1. Experimental investigation of the compression behaviour of polyurethane foam; **left:** Stress-strain-curve of PUR-cubes including in situ CT scan (see orange dot) at constant strain levels; **right:** Stress-time-curve during entire specimen scan shows stress relaxation for constant strains during CT scan

Due to the high complexity of the foam structure and to a generate an optimised resolution of the CT scan, the edge length of the foam cubes was set to 10 mm. As a result, the mean pore size has a larger influence on the mechanical properties than with the use of standardised specimen (edge length of 50 mm according to DIN EN ISO 844). Therefore, the stress-strain response of different specimen is characterised by a scatter, leading to a variance of 11.7 %. The measured Young's modulus was determined with 67.5 MPa (± 7.95 MPa standard deviation). The in situ CT scan was performed six times between 0 and 10 % strain in thickness direction. During each measurement, the strain was kept constant. With an increasing load, a slight relaxation of the foam material was observed (Figure 1

right). Since, the CT-scans show very high resolutions with no blurrings or major artefacts, the morphology of the cell structure was not influenced by relaxation phenomena.

4. Modelling and simulation of the compression deformation

For numerical investigations, a cuboid $\Omega = [0, a] \times [0, b] \times [0, a]$ from the center of the unloaded foam structure was cut out, where the integers a and b define the size of the 3D image in voxels, see Figure 2 for an illustration. The region containing the compact material within the cuboid is then defined by a threshold value of the greyscale data. The size of the foam structure is at the limit of the tomographic resolution. Therefore, additional filters to improve the quality of the foam representation were applied. After denoising (ImageJ, remove outliners [7]) the material volume is clipped (ParaView, clip [8]) and its surface is extracted. A smooting filter is applied to obtain a clean surface grid of improved resolution.
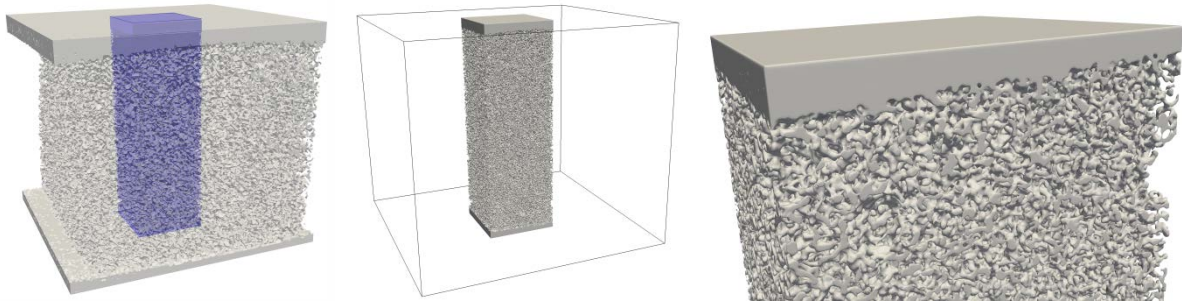
Figure 2. The foam geometry; **left:** Complete 3D geometry reconstructed from tomographic images; **middle:** Computational geometry Ω; **right:** Close-up to the computational geometry shows the fine structure

Instead of explicitly defining the complicated domain within this surface, the idea of the so-called diffuse domain approach was used [9]. This allows to solve the governing equations in the regular cuboidal domain Ω by using a phase-field describing the interior compact material implicitly. Thereby, the phase-field function ϕ is constructed such that $\phi \approx 1$ within the compact material and $\phi \approx 0$ in the air filled cavities. Here, the equation

$$\phi = 0.5 \left(1 - \tanh\left(\frac{3r(x)}{\epsilon} \right) \right) \tag{1}$$

was used, where $r(x)$ is the signed distance from a point $x \in \Omega$ to the surface of the compact material. The parameter ϵ controls the thickness of the transition layer where ϕ changes from 0 to 1. Finally, the regular cuboidal domain Ω is meshed using regular tetrahedral elements which are locally refined according to the phase-field function. A similar approach to use a phase-field to represent a complicated elastic domain has been used in [10], where more details on the method can be found. The compact material is assumed to be isotropic with unknown Young's modulus $E_{compact}$ and Poisson's ratio $\nu_{compact} = 0.35$. The foam deformation is described by the displacement vector u. Using the diffuse domain approach [9, 10], the governing equation for u can be written as

$$\nabla \cdot (\phi \sigma^*) = 0 \quad \text{in } \Omega. \tag{2}$$

The nondimensional material stress tensor σ^* is introduced to account for the unknown $E_{compact}$ and is defined such that the dimensional stress $= E_{compact}\sigma^*$, hence

$$\sigma^* = \mu^*(\nabla u + \nabla u^T) + \lambda^* I \nabla \cdot u \tag{3}$$

where I is the identity matrix and μ^*, λ^* are the Lamé coefficients divided by $E_{compact}$,

$$\mu^* = \frac{1}{2(1+\nu_{compact})}, \qquad \lambda^* = \frac{\nu_{compact}}{(1+\nu_{compact})(1-2\nu_{compact})}. \tag{4}$$

Using matched asymptotic analysis it can be shown that Eq. (2) converges to the equations of linear elasticity inside of the compact material when ϵ tends to zero [9]. The following Dirichlet boundary conditions were imposed

$$u = (0,0,0)\text{mm} \qquad \text{on } (\delta\Omega)_{\text{bottom}} \tag{5}$$

O. Weißenborn, S. Geller, M. Gude, F. Post, S. Praetorius, A. Voigt, S. Aland

$$\boldsymbol{u} = (0.12, -0.37, 0)\text{mm} \quad \text{on } (\boldsymbol{\delta\Omega})_{\text{top}} \tag{6}$$

which corresponds to the experimentally imposed compression of the foam by 4.2 % in the thickness-direction together with a slight tilt in the x-direction that can be seen in the tomographic images. At the remaining boundaries of Ω we assume no outer forces and set

$$\boldsymbol{\sigma}^* \cdot \boldsymbol{n} = \boldsymbol{0} \tag{7}$$

where **n** is the normal to $\delta\Omega$.

The resulting system is solved using an adaptive Finite Element method, with a fine grid resolution in the transition region of the phase-field, such that approximately 5 grid points are within a cross-section of the interface. The system of linear equations involves approximately 100 million degress of freedom and is solved by the iterative solver BiCGstab(ℓ=3), implemented in the software AMDiS (Adaptive MultiDimensional Simulation) on 112 cores in parallel [11, 12].

5. Discussion of numerical results

To evaluate the results, an xy-slice of the 3D-domain through the center of the cuboid was considered. The compact material is visualized by the ensemble of points for which $\boldsymbol{\phi} > 0.5$. This domain is warped by the calculated displacement field to compare experimental and numerical morphology in Figure 3.
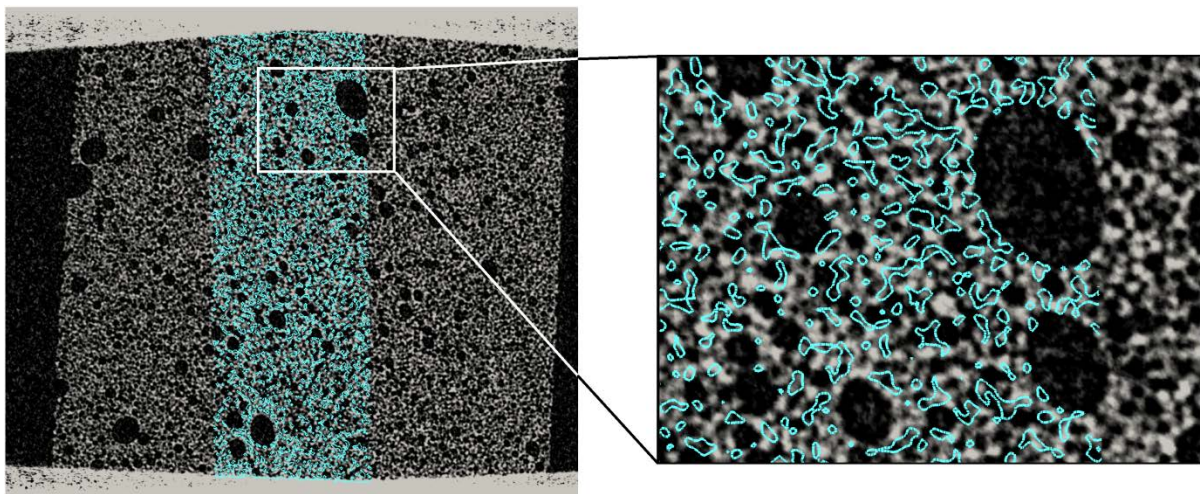
Figure 3. Comparison between experimental (background) and numerical (contour lines) morphology of the deformed configuration for 4.2 % vertical compression; **left:** The overall configuration shows very good agreement, particularly at the pores; **right:** A close-up shows expected differences in the small-scale structures, which might result from slight uncertainties in the slice position (see text)

Overall, very good agreement was observed, in particular the position of the larger air cavities matches very well to the experimental image. Due to the complexity of the scaffold, the agreement for small-scale structures is expected to be lower. In fact, a slight deviation from the slice position can already result into a completely different morphology. An advantage of the numerical computations is the analysis of local material properties. In Figure 4 the volumetric strain $\nabla \cdot \boldsymbol{u}$ is shown which corresponds to the local amount of compression. Laterally around the larger air cavities, local compressions of up to 6 % can be observed. Below and above some cavities slight stretching of up to 1 % can take place.

O. Weißenborn, S. Geller, M. Gude, F. Post, S. Praetorius, A. Voigt, S. Aland
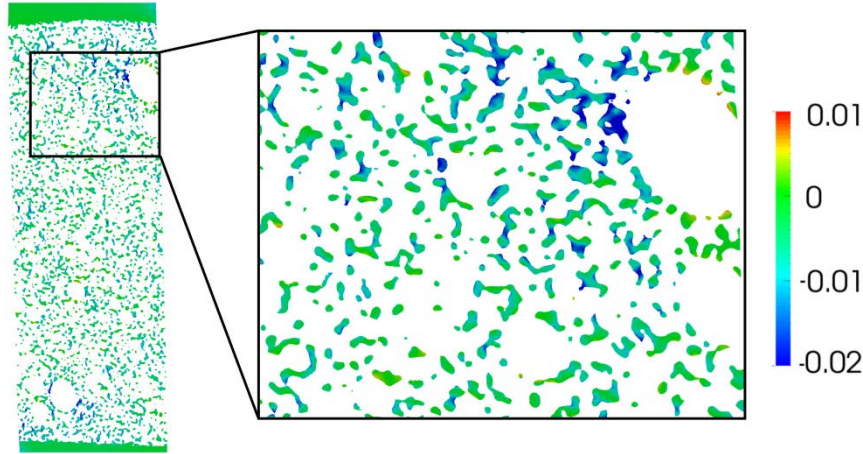
Figure 4. Volumetric strain $\nabla \cdot \boldsymbol{u}$ shows the local amount of relative compression. Obtained strain values are between -0.06 and 0.01, but the scale is restricted to [-0.02, 0.01] for better visibility.

In order to obtain the homogenized material parameters of the foam ($\boldsymbol{\nu}_{\textbf{foam}}, \boldsymbol{E}_{\textbf{foam}}$), the simulation results can be matched to a homogeneous elastic material. Given the imposed Dirichlet boundary conditions, the calculated displacement field is independent of the Young's modulus. By making use of this property, the Poisson's ratio $\boldsymbol{\nu}_{\textbf{foam}}$ can be computed. Assuming a homogeneous material by setting $\boldsymbol{\phi} = 1$, Eq. (2) can be solved for different Poisson's ratio $\boldsymbol{\nu}_{\textbf{foam}}$ (varied in steps of 0.01) that now replace $\boldsymbol{\nu}_{\textbf{compact}}$. To match the obtained displacement to the displacement of the experimental structure, the absolute change in material volume was compared

$$\Delta V = \int_{\Omega} \nabla \cdot \boldsymbol{u} \, \textbf{dV}. \tag{8}$$

The volume change of the porous structure is $\Delta V = -1.16909 \, mm^3$. This value is most closely approximated by a homogeneous structure with $\nu_{\text{foam}} = 0.33$. To obtain the homogenized Young's modulus, the nondimensional stress acting on the top boundary is computed,

$$\boldsymbol{f}^* = \frac{\int_{(\delta\Omega)_{\textbf{top}}} \phi\sigma^* \cdot \boldsymbol{n} \, \textbf{dA}}{\int_{(\delta\Omega)_{\textbf{top}}} \textbf{1} \, \textbf{dA}}, \tag{9}$$

for the homogenized simulation with $\nu_{\text{foam}} = 0.33$ and $|\boldsymbol{f}^*| = 0.0386$ was obtained. The stress is related to the dimensional stress $|\boldsymbol{f}| = 2.1$ MPa (see Figure 1 left), by the relation $\boldsymbol{f} = E_{\text{foam}}\boldsymbol{f}^*$. The calculated effective modulus $E_{\text{foam}} = 55$ MPa agrees relatively well with experimentally measured values of 67.5 MPa. Beyond that, the influence of the porosity on the elastic response of the foam was investigated. The material volume fraction $\chi = 0.21$ was obtained in agreement with the experimental measurements. A small shift r_0 in the signed distance function allows to change the thickness of the elastic structures, and hence the material fraction. Accordingly, Eq. (1) was replaced by

$$\boldsymbol{\phi} = \textbf{0.5} \left(\textbf{1} - \tanh\left(\frac{\textbf{3}(r(x)+r_0)}{\epsilon}\right) \right), \tag{10}$$

such that less compact material for $r_0 \geq 0$ and more compact material for $r_0 \leq 0$ was obtained. Figure 5 shows the scaffold for different r_0, which corresponds to different material volume fractions χ.

O. Weißenborn, S. Geller, M. Gude, F. Post, S. Praetorius, A. Voigt, S. Aland
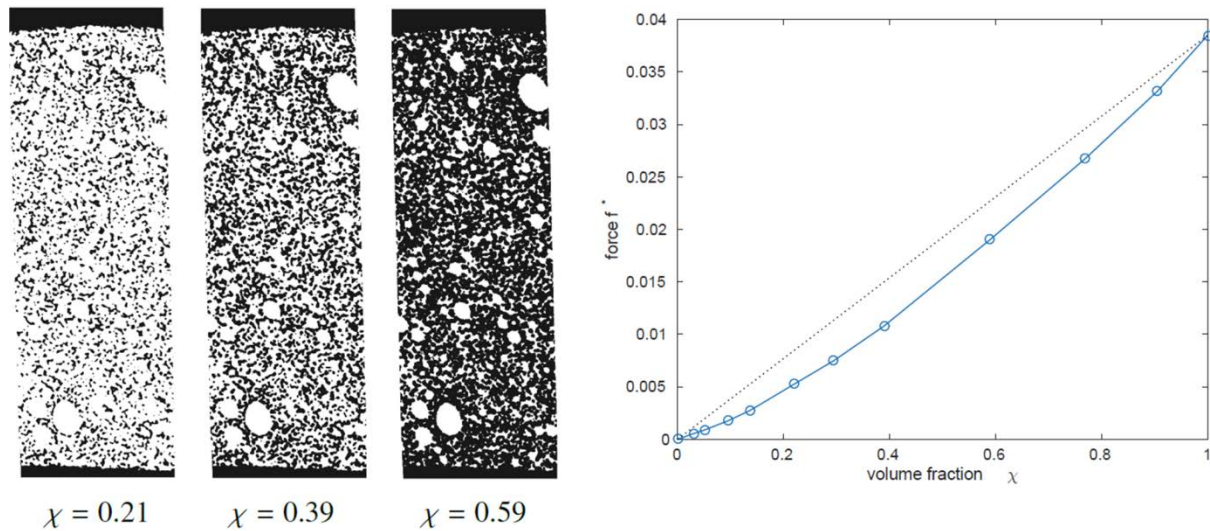
Figure 5. Effect of porosity on the stiffness of the foam structure; **left:** Centered slice through the structure for different volume fractions χ; **right:** Numerically computed elastic modulus of the structure (blue) is not a simple linear function (grey dotted) of material volume fraction.

The force necessary to compress the foam can be computed from numerical simulations. This force and hence the elastic modulus of the foam was found not to be a simple linear function of material volume fraction, but rather a slightly progressive correlation. This correlation is in good agreement with experimental investigations on the density-related effective compression modulus of polyurethane rigid foam (Figure 6).
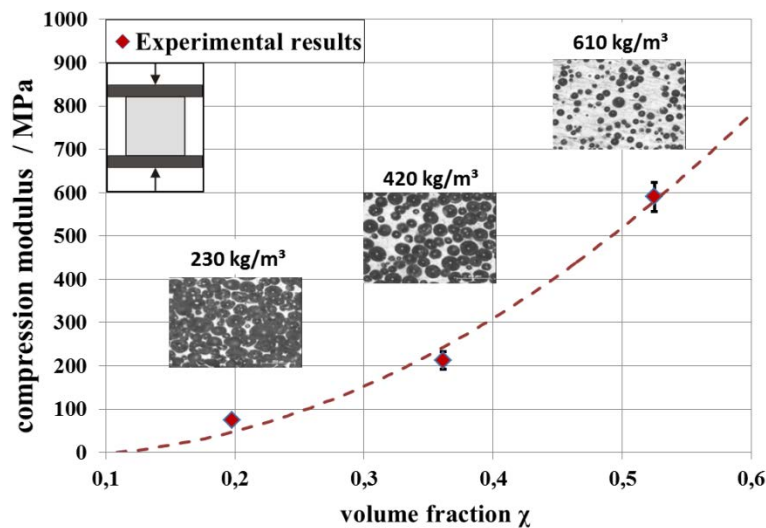
Figure 6. Density-related compression modulus of PUR-foam

6. Conclusions

With the use of the in situ CT, valuable information on the local deformation of complex polymer foams under compression load could be obtained. The developed phase-field function to implicitly describe the foam structure allows the calculation of global deformations and the local strain distribution. These numerical results are in good agreement with experimental results, although small-scale structures are expected to have a lower consistency due to the complexity of the scaffold and a slight deviation of the slice position. However, the model is able to calculate local strains within the compact material, allowing to predict possible damage initiation spots. Future work will validate this simulation method for further loading scenarios, such as tension and shear, and focus on generating a higher quality on small-scale structures of the foam.

O. Weißenborn, S. Geller, M. Gude, F. Post, S. Praetorius, A. Voigt, S. Aland

References

[1] R. Böhm, J. Stiller, T. Behnisch, M. Zscheyge, R. Protz, S. Radloff, M. Gude and W. Hufenbach, "A quantitative comparison of the capabilities in in siut computed tomography and conventional computed tomography for damage analysis of composites," *Composites Science and Technology, vol. 110,* pp. 62-68, 2015.

[2] Y. Nikishkov, G. Seon, A. Makeev and B. Shonkwiler, "In-situ measurements of fracture toughness properties in composite laminates," *Materials & Design, vol. 94 (15),* pp. 303-313, 2016.

[3] E. Ciecierska, M. Jurczyk-Kowalska, P. Bazarnik, M. Gloc, M. Kulesza, M. Kowalski, S. Krauze and M. Lewandowska, "Flammability, mechanical properties and structure of rigid polyurethane foams with different types of carbon reinforcing materials," *Composite Structures, vol. 140,* pp. 67-76, 2016.

[4] D.-A. Serban, O. Weissenborn, S. Geller, L. Marsavina and M. Gude, "Evaluation of the mechanical and morphological properties of long fibre reinforced polyurethane rigid foams," *Polymer Testing 49,* pp. 121-127, 2016.

[5] V. Alstädt and G. Krausch, *Special issue - Polymer foams, vol. 56,* pp. 3-4, 2015.

[6] D. Whisler and H. Kim, "Experimental and simulated high strain dynamic loading of polyurethane foam," *Polymer Testing, vol. 41,* pp. 219-230, 2015.

[7] W. Rasband, "Imagej," U.S. National Institutes of Health, Bethesda, Maryland, USA, 1997-2015.

[8] U. Ayachit, "The paraview guide: A parallel visualization application.," 2015.

[9] X. Li, J. Lowengrub, A. Rätz and A. Voigt, "Solving PDEs in complex geometries: A diffuse domain approach," *Comm. Math. Science, vol. 7 (1),* pp. 81-107, 2009.

[10] S. Aland, C. Landsberg, R. Müller, F. Stenger, M. Bobeth, C. Langheinrich and A. Voigt, "Adaptive diffuse domain approach for calculating mechanically induced deformation of trabecular bone.," *Computer methods in biomechanics and biomedical engineering, 17.1,* pp. 31-38, mar 2014.

[11] S. Vey and A. Voigt, "Amdis: Adaptive multidimensional simulations," *Computing and Visualization in Science, vol. 10 (1),* pp. 57-67, 2007.

[12] T. Witowski, S. Ling, S. Praetorius and A. Voigt, "Software concepts and numerical algorithms for a scalable adaptive parallel finite element method," *Advances in Computational Mathematics, vol. 41 (6),* pp. 1145-1177, 2015.

O. Weißenborn, S. Geller, M. Gude, F. Post, S. Praetorius, A. Voigt, S. Aland